

My Smartphone Knows What You Print: Exploring Smartphone-based Side-channel Attacks Against 3D Printers

Chen Song, Feng Lin, Zongjie Ba, Kui Ren, Chi Zhou, Wenyao Xu
SUNY at Buffalo, Buffalo, NY, USA
Email: {csong5, flin7, zba2, kuiren, chizhou, wenyaoxu}@buffalo.edu

ABSTRACT

Additive manufacturing, also known as 3D printing, has been increasingly applied to fabricate highly intellectual property (IP) sensitive products. However, the related IP protection issues in 3D printers are still largely underexplored. On the other hand, smartphones are equipped with rich onboard sensors and have been applied to pervasive mobile surveillance in many applications. These facts raise one critical question: is it possible that smartphones access the side-channel signals of 3D printer and then hack the IP information? To answer this, we perform an end-to-end study on exploring smartphone-based side-channel attacks against 3D printers. Specifically, we formulate the problem of the IP side-channel attack in 3D printing. Then, we investigate the possible acoustic and magnetic side-channel attacks using the smartphone built-in sensors. Moreover, we explore a magnetic-enhanced side-channel attack model to accurately deduce the vital directional operations of 3D printer. Experimental results show that by exploiting the side-channel signals collected by smartphones, we can successfully reconstruct the physical prints and their G-code with Mean Tendency Error of 5.87% on regular designs and 9.67% on complex designs, respectively. Our study demonstrates this new and practical smartphone-based side channel attack on compromising IP information during 3D printing.

1. INTRODUCTION

After decades of development, additive manufacturing (AM), also known as 3D printing, has been becoming a mainstream manufacturing process in various industry fields. Specifically, it refers to a process by which 3D digital design data (in the cyber domain) is used to build up a 3D physical object in layers by depositing material (in the physical domain). Compared with the conventional manufacturing techniques, 3D printing has the following advantages: 1) efficiency: fast and cost-efficient production with less waste material; 2) creativity: flexible with more complex geometries construction; 3) accessibility: affordable price of 3D

printers and materials. The global value of 3D printing is estimated to reach over 20.2 billion dollars by 2021 [42].

With the wide expansion of 3D printing and new merging materials in application fields, there are increasingly more highly intellectual-property (IP) sensitive products manufactured by 3D printers. Key industries, such as medical [26, 17], aerospace [15, 28] as well as biomedical sectors [39, 37], contain confidential IP from personal health-care to national strategic products. Therefore, IP security in the 3D printing process chain has received increasing attention in the last two years. Specifically, 3D printing can be divided into the cyber domain and the physical domain. In 2014, Strum *et al.* [38] raised the idea of cyber-vulnerability in 3D printing where a malicious software can alter design files. Later on, many security technologies such as encryption and watermark, were adopted to protect IP in the cyber domain [13, 19]. However, IP protection in the physical domain of 3D printing is still underexplored.

Considering that smartphones are equipped with a rich set of on-board sensors, we ask one question: *is it possible to infer IP information when a smartphone is placed nearby and record side-channel signals during the 3D printing process?* This question raises a potentially more serious concern on IP protection issues in 3D printing. Compared with professional devices, smartphones are more commonly used and accessible in daily life, and the side-channel attack using a smartphone can be inconspicuously launched because of its portability and pervasiveness. This observation motivates us to investigate the IP leakage potential in side channels of 3D printers using commercial off-the-shelf smartphones.

In this paper, we perform an end-to-end study on exploring smartphone-based side-channel attacks against 3D printers. We formulate the IP definition and attack protection problem in the 3D printing application. These formal definitions can systematically evaluate potential attacks and guide defense models. After that, we analyze the working mechanism of 3D printers in-depth and reveal the possible side channels and their relationship to the 3D design information. During the printing process, multiple electromechanical parts in 3D printers will emit diverse side-channel signals according to the G-code instructions, which contain the 3D design information. Accordingly, we investigate multiple side channels (e.g., acoustic and magnetic signals) and develop a fusion model to infer the 3D digital design. Experiment results show that by exploiting the side-channel information collected by a smartphone, we can successfully reconstruct the physical prints and their G-codes with the Mean Tendency Error of 5.87% on regular designs and 9.67%

Permission to make digital or hard copies of all or part of this work for personal or classroom use is granted without fee provided that copies are not made or distributed for profit or commercial advantage and that copies bear this notice and the full citation on the first page. Copyrights for components of this work owned by others than ACM must be honored. Abstracting with credit is permitted. To copy otherwise, or republish, to post on servers or to redistribute to lists, requires prior specific permission and/or a fee. Request permissions from [permissions@acm.org](http://permissions.acm.org).

CCS'16, October 24-28, 2016, Vienna, Austria

© 2016 ACM. ISBN 978-1-4503-4139-4/16/10...\$15.00

DOI: <http://dx.doi.org/10.1145/2976749.2978300>

on complex designs. Our study reveals that IP protection in the 3D printing process deserves more attention, especially in the era of smartphones and internet of things.

To the best of our knowledge, ours is the first study to explore practical side-channel attacks on 3D printers via the smartphone. Our contributions are summarized as follows:

- We formalize IP information and side-channel attack problem in 3D printing.
- We analyze the 3D printing mechanism and explore multiple side-channel attacks against 3D printers via the smartphone.
- We validate the feasibility and effectiveness of the smartphone-based side-channel attack against 3D printers in a real case study.
- We discuss a few defense mechanisms to improve the design of IP protection in 3D printing against side-channel attacks.

The rest of this paper is organized as follows: we introduce the background of 3D printing and formulate the related side-channel IP attack problem in Section 2. We investigate the acoustic and magnetic side channels in Section 3 and Section 4 respectively. Based on the analysis, we discover a smartphone-based side-channel attack in Section 5. We evaluate the performance of the approach in Section 6. Afterwards, we discuss limitation and describe future work in Section 7. The defense mechanism is explored in Section 8. We review the related work in Section 9. The work is summarized in Section 10.

2. PRELIMINARIES AND PROBLEM FORMULATION

2.1 3D Printing Overview

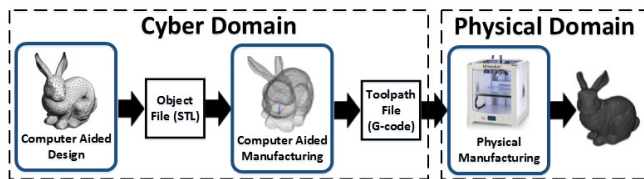


Figure 1: The 3D printing chain includes the cyber domain and the physical domain.

As shown in Figure 1, a standard 3D printing chain comprises the cyber domain and the physical domain. First, the designer creates the object model in CAD (computer aided design) software. The CAD software converts the CAD model into the standard object file (STL), where the model is represented by the surface geometry composed of triangular facets. Second, after receiving the STL file, the CAM (computer aided manufacturing) module slices the model into uniform layers and generates the toolpath file. G-code is the most widely used toolpath file format [11]. It includes the operational instructions of 3D printers to control the fabricating process. In other words, G-code naturally contains all IP information of the 3D digital design, such as shapes, dimensions and volumes. Last, the 3D printer conducts the physical manufacturing and fabricates the object. In this

study, we investigate 3D printers based on the Fused Deposition Modeling (FDM) technology because it is the most commonly used type in the cost-effective 3D printing market [29].

2.2 3D Printing Mechanism

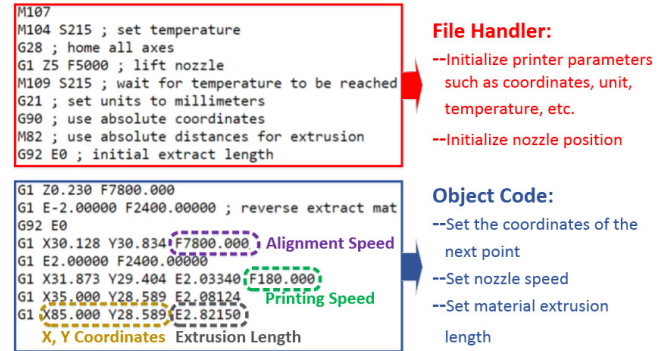


Figure 2: The semantic structure of a real 3D printing G-code, which contains the file handler as well as the object code.

Figure 2 shows a G-code example for an object, which contains the file handler as well as the object code. The file handler initializes the printer settings including unit, coordinates, temperature, etc. In the object code section, each instruction line controls the printer to perform certain operations. Since it is fully compatible with commercial 3D printers, successful IP attacks on the G-code will directly result in the IP leakage and product replication. Considering that the G-code has a one-to-one relationship with the printer operation, we plan to obtain the G-code by investigating the mechanism of the printer operations.

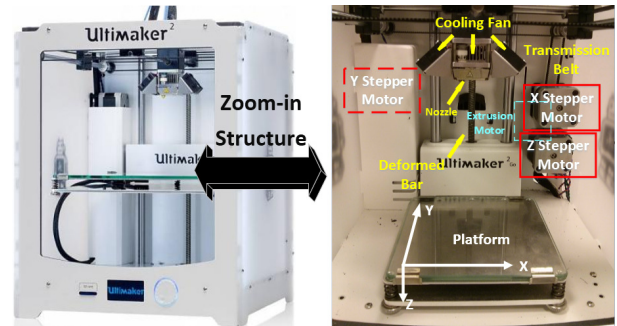


Figure 3: A 3D FDM printer (Ultimaker 2 Go) and its inner physical structure, including stepper motors, a heating nozzle, cooling fans and actuation systems (transmission belt and deformed bar).

A typical FDM 3D printer is shown in Figure 3. The printing header is placed at the top of the printer and can only move in the horizontal plane. A nozzle is located at the bottom of the header. A platform stays in the middle and can move vertically. The coordinates of the platform are illustrated in the figure. When the printing process starts, the platform is raised up to an initial height (the first layer) along the Z axis. After the first layer is printed in the X-Y plane, the platform moves down by one layer height and

the printer prints the next layer upon the first one. This process continues till the end when the last layer is finished. Particularly, there are four primitive operations involved. Layer Movement infers whether the printer prints the layer in the X-Y plane or changes layer in the Z axis. When the printer prints in the X-Y plane, Header Movement determines whether the header moves at the printing speed or aligns the position with a fast speed. Axial Movement corresponds with the specific axis the nozzle moves along with in the X-Y plane. In each axis, the nozzle can move in two directions, which is identified by Directional Movement. During printing, the nozzle will be heated to change the state of the material from solid into quasi-solid. Cooling fans are equipped next to the nozzle to control its temperature. There are four stepper motors, where three motors control the platform or nozzle movement in different axes and the fourth one (extrusion motor) extrudes the material. The printing operations are controlled by four motors via the actuation systems. In summary, the primitive printer operations are listed as follows:

- Layer Movement: whether the printer prints in a layer or change to the next layer;
- Header Movement: whether the header prints object or aligns position;
- Axial Movement: whether the nozzle moves in X or Y axis in the X-Y plane;
- Directional Movement: which direction the nozzle moves in the X or Y axis;

As described above, there are a few different eletromechanical parts in 3D printers. These parts will generate a set of side-channel signals during the 3D printing process. Given the ubiquity of smartphones, these observations motivate us to explore the possible side-channel attacks against 3D printing through smartphone built-in sensors.

2.3 Definition and Problem Formulation

In this part, we begin by defining the key terms in the 3D printing study. We also formulate the side-channel IP attack problem.

2.3.1 Terminologies

Definition 1 (IP Pile and IP Set): For a 3D printing process, let s denote the IP pile that is achieved by certain attack method. We define IP set S as a set that contains all possible IP piles. Specifically, we define s_0 be the complete IP pile that has all the information about the design and the 3D printing process (the complete G-code). Therefore,

$$\forall s \in S, \emptyset \subset s \subseteq s_0. \quad (1)$$

Figure 4 shows two examples of s . The left one is the complete G-code (s_0) and the right one is the partial G-code where part of the information is lost.

Definition 2 (Side-channel Pile): Let \hat{u} be the side-channel data pile collected by the smartphone’s built-in sensors. Correspondingly, it contains multiple side-channel signals in time series. Specifically, we define u_0 to be the complete side-channel pile containing all possible side-channels that are accessible by the smartphone. Therefore,

$$\hat{u} \subseteq u_0. \quad (2)$$

Figure 5 is an example of the collected side-channel pile, which contains the timestamp as well as the side-channel signals.

The figure shows two side-by-side boxes representing G-code. The left box contains the complete G-code for a layer, listing various G1 commands with X, Y, Z coordinates and feed rates. The right box shows the same G-code but with a large section of the middle commands obscured by a black hatched pattern, representing a partial G-code where information is lost.

Figure 4: Two examples of s . The left one is the complete G-code and the right one is the partial G-code.

Time-stamp	Side-channel Signals		
	Magnetic _x	Magnetic _y	Magnetic _z
118,	-0.0434417,	0.2357025,	9.111877, ...
129,	-0.0410614,	0.2535553,	9.089264, ...
140,	-0.0410614,	0.2535553,	9.089264, ...
150,	0.0374908,	0.3213958,	9.205902, ...
160,	0.0529632,	0.2833099,	9.161865, ...
170,	0.0446319,	0.2583160,	9.205902, ...

Figure 5: An example of u , which is the side-channel pile collected by the smartphone’s built-in sensors.

Definition 3 (Status Analysis Function): We denote the status analysis function p as any function which can analyze the 3D printer status at a specific timestamp. Therefore, let P be a set which contains a number of selected status analysis functions:

$$P = \{p_1(), \dots, p_k()\}. \quad (3)$$

Definition 4 (IP Conversion Function): Let $Q()$ be a mapping function which converts a series of 3D printer status into the standard IP pile (G-code). The specific implementation of $Q()$ responds to the G-code grammar and mechanism of the 3D printer design.

2.3.2 Problem Formulation

Formulation 1 (Printing Plan Extraction): The goal of printing plan extraction is to extract the mechanical and the product-related information from the collected side-channel pile U . Specifically, a status analysis function set P is applied. We define A be the result set after applying P on \hat{u} :

$$A = \{a_1 \leftarrow p_1(U), \dots, a_k \leftarrow p_k(U)\}. \quad (4)$$

Therefore, A is the integration set of 3D printer status in time series. It contains information such as the nozzle coordinates, the platform height, the printing speed, the temperature, etc.

Formulation 2 (IP Reconstruction): The purpose of IP reconstruction is to achieve the reconstructed IP pile (s) from the 3D printer status collection A using IP conversion function $Q()$. Specifically, Let $s_{IP-Leak}$ be the reconstructed IP pile obtained by the attacker. Therefore,

$$s_{IP-Leak} = Q(A) \subseteq s_0. \quad (5)$$

Formulation 3 (IP Attack Assessment): We verify the reconstructed IP pile $s_{IP-Leak}$ and assess the 3D printing IP attack into two levels. Specifically, we compare $s_{IP-Leak}$ with the original IP set s_0 . We term **Full IP Attack** and **Partial IP Attack** as follows:

$$s_{IP-Leak} \begin{cases} = s_0 & \Rightarrow \text{Full IP Attack} \\ \subset s_0 & \Rightarrow \text{Partial IP Attack} \end{cases} \quad (6)$$

2.4 Threat Model

After formulating the problem, we describe the adversary attacking scenario and goal. Suppose a design is printed by a 3D printer and the attacker attempts to obtain the original IP pile s_0 of the design for illegal usage. The attacker does not have any prior knowledge about the target printer and therefore, can be any common people with a smartphone. After entering the space where the 3D printer locates, the attacker places the smartphone near the printer to collect side-channel information. Note that the smartphone does not need any physical contact with the printer. This is completely unsuspecting due to the pervasiveness of the smartphone nowadays and it is normal for people to place their smartphones on the table. With the recording application running on the smartphone, the attacker does not even need to be at scene. During the printing process, the smartphone records the side channel data simultaneously. Once the printing process is finished, the attacker fetches the smartphone and obtains the side-channel data pile \hat{u} . After applying the well-selected printer status analysis functions, the attacker integrates the printer status \mathbf{A} in time series. In the end, the attacker performs the IP reconstruction using IP conversion function $Q()$ to retrieve the IP pile $s_{IP-Leak}$ of the design. If $s_{IP-Leak}$ is the same as s_0 , then the attacker performs a **Full IP Attack**. Otherwise, it is a **Partial IP Attack**. The attack is unobtrusive and easy to launch.

3. EXPLORING ACOUSTIC SIDE CHANNEL

The determination of printer operations, especially the axial and directional movements of the nozzle, is of great importance to reconstruct the product’s contour in each layer as well as the design IP. There are four basic nozzle movements with respect to the axis and the direction: X-Left, X-Right, Y-Up, Y-Down. In this section, we validate whether the smartphone’s acoustic data can be utilized to deduce the movements.

To conduct the validation, we implement an application on Nexus 5 (Android OS v6.01) to collect the acoustic data. We separate the data into the training and the testing set. Specifically, we train a support vector machine (SVM) model based on the training set and evaluate the performance on the testing set. The detailed experiment setup is described in Section 4. Figure 6 depicts the validation results. The classifier well predicts the axial Movement, but poorly detects the directional Movement in each axis. There are lots of mis-classification between X-Left and X-Right, or Y-Up and Y-Down. To well understand the result, we first analyze how the stepper motor operates and how it controls the nozzle movement.

The stepper motor effectively has multiple “toothed” electromagnets arranged around a central gear-shaped piece of

		Predicted Label			
		X-Right	X-Left	Y-Down	Y-Up
True Label	X-Right	51.30%	39.80%	2.90%	6.00%
	X-Left	33.90%	61.10%	2.00%	3.00%
	Y-Down	3.90%	2.40%	69.70%	24.00%
	Y-Up	10.40%	4.30%	27.00%	58.30%
		X-Right	X-Left	Y-Down	Y-Up

Figure 6: The model accuracy when the acoustic data is applied to deduce Axial and Directional Movement in 3D printing.

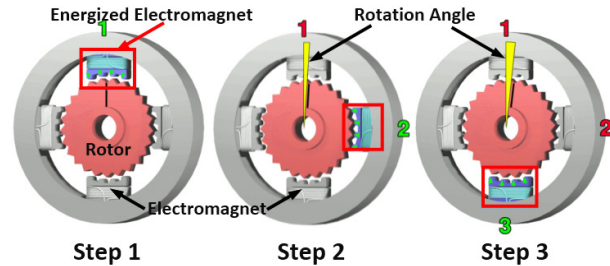


Figure 7: The illustration of how the stepper motor works. The electromagnet in the red rectangle is the energized one. Others in gray are un-energized.

iron, called rotor. To make the motor turns, first electromagnet is given power, which magnetically attracts the rotor’s teeth. When the rotor’s teeth are aligned to the first electromagnet, they are slightly offset from the next electromagnet. This means that when the next electromagnet is turned on and the first is turned off, the rotor rotates slightly to align with the next one. This process is repeated afterwards. In this way, the motor can be turned by a precise angle (see in Figure 7). Therefore, if the motor holds still, it means the printer maintains the activated electromagnet to stabilize the rotor and the nozzle holds still as before. When the motor rotates in a direction, it controls the nozzle movement through two independent sets of transmission belts, which have different mechanical structures. Specifically, the movement direction changes when the energized order of the electromagnet reverses.

The nozzle axial movement in X or Y axis generates distinguishable sound because each motor and the corresponding actuation set are in different structures. The directional movement on the same axis (i.e., up or down, left or right), on the other hand, is determined by the configuration of the energized order in the electromagnet and the belt rotation. Therefore, the directional movement is much challenging to

deduce based on the smartphone’s acoustic data because the reverse configuration produces similar sound.

A recent study [12] is in coherence with our observation from a different angle. Zoom H6 Acoustic Recorder [10] was employed to collect the subtle difference of the vibration (frame energy) conducted from the motor to the nozzle when the nozzle moved in two directions in one axis. As a professional recorder, Zoom H6 is much more powerful in the recording capability when compared to the smartphone. Table 1 lists the main differences in the specifications. Therefore, it is difficult for the smartphone to well detect such subtle directional information and we need to explore other side channels.

	Zoom H6	Nexus 5
Mic Type	Uni/bi/Omni-directional	Omni-directional
Channel Number	8	2
Sampling Freq.	96KHz	44.1KHz
Encoding Bit-rate	24bit	16bit

Table 1: Specification comparison between the microphones on Zoom H6 and Nexus 5.

4. EXPLORING MAGNETIC SIDE CHANNEL AND BEYOND

The mechanism of the stepper motor inspires us to explore the relationship between the magnetic side channel and the nozzle movement. Therefore, we perform pilot experiments to investigate the magnetic field from the smartphone’s perspective of view when the nozzle conducts the directional movement in X or Y axis.

4.1 Magnetic Side Channel and Directional Movement

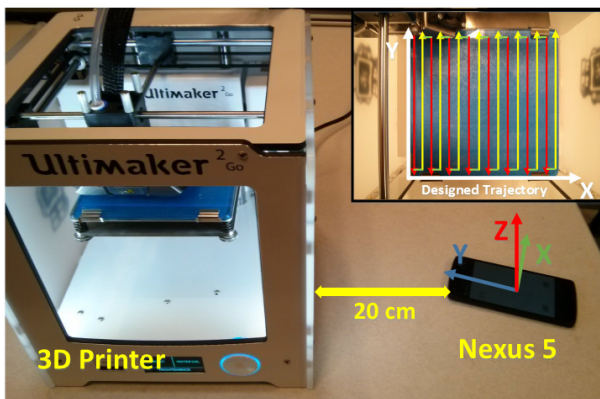


Figure 8: The experiment setup to explore the magnetic side channel. Specific trajectory is designed to investigate the relationship between the directional movement and the magnetic side channel. The coordinates of the smartphone as well as the 3D printer are plotted respectively.

We implement the sensor data collection application on Nexus 5 with Android OS 6.01. As shown in Figure 8, the smartphone is placed on the table to collect the magnetic

data. The smartphone’s built-in sensors have their own coordinates, which are high-lighted in the figure. Due to the limitation in space, we only show the study in one axis for the purpose of demonstration. We design a specific trajectory which mainly contains two directional movements in the Y axis: Y-Up and Y-Down. The recording rate of the magnetic sensor data was 100Hz.

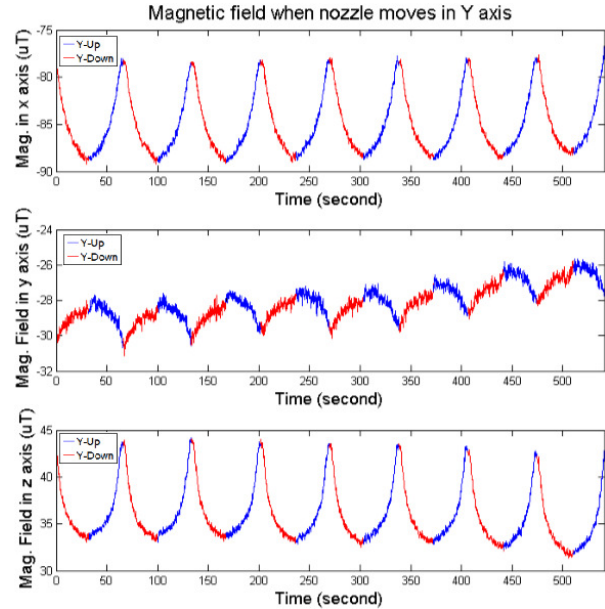


Figure 9: The detected magnetic data when the nozzle operates the directional movement in the Y axis. Specifically, Y-Up is colored in red and Y-Down is colored in blue.

As depicted in Figure 9, we plot the magnetic data in each sensor coordinate, respectively. Specially, the red segment refers to Y-Up and the blue one refers to Y-Down. Interestingly, distinguishable patterns in the magnetic field are observed. When the nozzle operates one typical directional movement (either Y-Up or Y-Down), the detected magnetic data in each coordinate demonstrates high degree of consistency in the signal pattern. The drift in the pattern when the nozzle moves from one side of the platform to the other does not affect the overall tendency. The directional movement in the X axis also shows the similar result in the magnetic data. Therefore, magnetic side channel contains rich information to deduce the directional movement.

4.2 Magnetic Channel Model

We utilize the magnetic side channel to predict the nozzle directional movement. Specifically, we train the magnetic channel model based on the magnetic data using support vector machines (SVM). Feature extraction is conducted to better represent the original signal in the feature space.

Feature Extraction.

We extract a set of features to characterize the signal’s directional behavior in both the temporal and spectral domains. Specifically, the temporal features are computed from the waveform of the magnetic field signal, while spectral features are acquired performing a P-point Fast Fourier

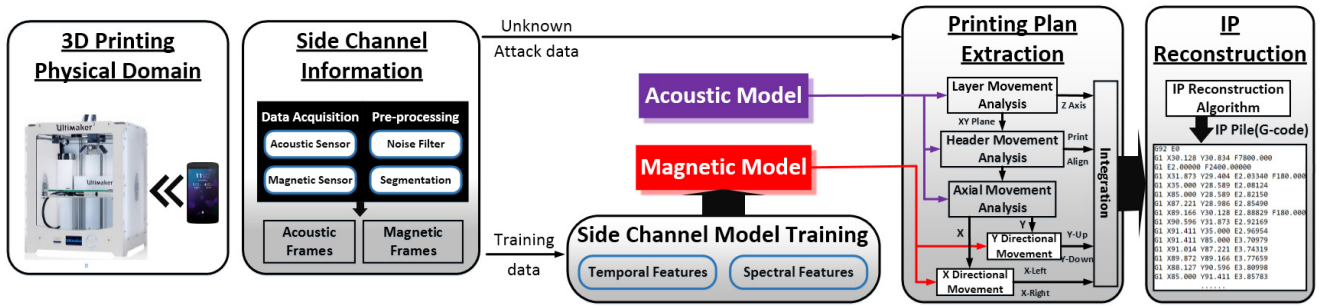


Figure 10: The proposed magnetic-enhanced IP side-channel attack framework against 3D printers. It demonstrates an end-to-end framework from side channel information acquisition to IP reconstruction.

Transform to each signature of the magnetic field signal [40]. In the temporal domain, we investigate the signal tendency by deriving the velocity and the averaged first order derivative. Other features, such as interquartile range, zero crossing rate, mean crossing rate, skewness and kurtosis, reflect the distribution of the signal.

Particularly, for a given signal frame X , interquartile range (IQR) measures the statistical dispersion within each segmentation, which is the difference between 75th and 25th percentiles of the signal over the window:

$$IQR = \text{mean}[X(\frac{n}{2} : \frac{3n}{4})] - \text{mean}[X(1 : \frac{n}{4})]. \quad (7)$$

Skewness is a measure of the asymmetry of the probability distribution of the real-valued data:

$$\gamma = \frac{E[(X - \mu)^3]}{(E[(X - \mu)^2])^{3/2}}, \quad (8)$$

where μ is the mean and E is the expectation operator.

Similarly, kurtosis is a descriptor of the shape of a probability distribution and refer to the degree of asymmetry and peakedness of the signal distribution:

$$Kurt = \frac{E[(X - \mu)^4]}{(E[(X - \mu)^2])^2}. \quad (9)$$

Besides, we calculate the correlation between each pair of the sensor coordinates:

$$\text{corr}(X, Y) = \frac{E[(X - \mu_X)(Y - \mu_Y)]}{\sigma_X \sigma_Y}, \quad (10)$$

where σ_X, σ_Y are standard deviations.

In the spectral domain, we explore the spectral energy and entropy, which measure the energy changes in signal and infer the motion difference. Let $xfft_i, i = 1, \dots, n$ be the Fast Fourier Transform (FFT) coefficient of X .

$$\text{Energy}(X) = \frac{1}{n} \sum_2^{n-1} (2 * xfft_i). \quad (11)$$

For spectral entropy, which is defined as the normalized information entropy of the discrete FFT component magnitudes of the signal, we first divide the spectral $xfft$ into m sub bins $xfft(j), j = 1, \dots, m$ and normalize them by the number of bins. Therefore, Power Spectral Density is calculated as:

$$P(j) = \frac{1}{m} |xfft(m)|^2. \quad (12)$$

Then Probability Density Function can be derived by normalizing the calculated PSD:

$$p(j) = \frac{P(j)}{\sum_j P(j)}. \quad (13)$$

Hence, we can formulate the spectral entropy as:

$$SE = - \sum_{j=1}^m p(j) \log_2 p(j). \quad (14)$$

4.3 Acoustic Channel Model

Although acoustic side channel can not well distinguish the nozzle direction movement, it can still be effective in other aspects. The acoustic channel model is trained in the similar way as the magnetic one. However, we extract additional features to explore the features in the acoustic side channel. In the temporal domain, we further introduce parameters such as mean, median, standard deviation and variance [24] to represent the statistic features of the sound. In the spectrum domain, Mel-frequency cepstral coefficients (MFCC) are widely used in audio signal processing and proven to be effective [31, 30]. As a result, we also incorporate it into the feature set.

5. MAGNETIC-ENHANCED IP SIDE-CHANNEL ATTACK

In this section, we introduce a magnetic-enhanced side-channel approach to attack the 3D printing IP via smartphone in the physical layer. Figure 10 shows the proposed end-to-end framework from side channel information acquisition to IP reconstruction. The detail of each module is described as follows:

5.1 Side Channel Information

During the process of 3D printing, we collect the side-channel information via smartphone and pre-process the data for further analysis.

- Data Acquisition: We implement a smartphone recording application which can simultaneously and continuously collect the magnetic and acoustic data.
- Pre-processing: To remove the signal noise generated by other interferes as well as white noise, we apply Savitzky-Golay filter [34] on the collected data. Compared to the most common moving average filter, it is a much better procedure which performs a least squares

fit of a small set of consecutive data points to a polynomial and take the calculated central point of the fitted polynomial curve as the new smoothed data point. After that, we segment the signal into separate frames with a fixed frame size.

5.2 Primitive Operation Analysis

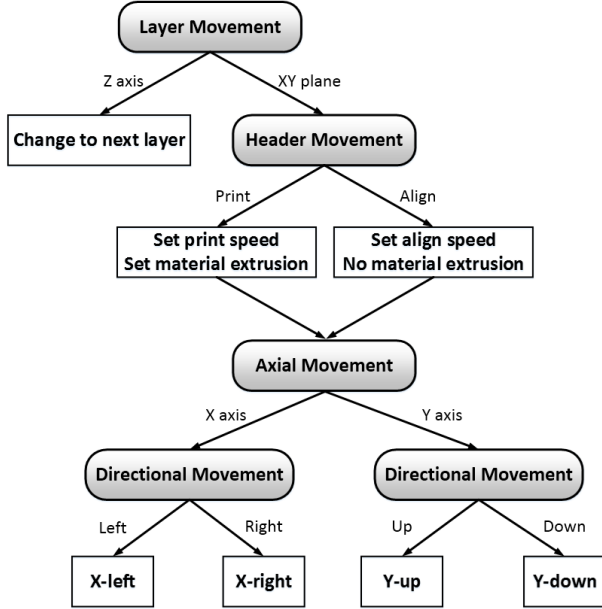


Figure 11: The hierarchy diagram shows the sequential relationship between the primitive operations based on the 3D printing mechanism.

In Section 2.2, we introduce the primitive operations in 3D printing: Layer Movement, Header Movement, Axial Movement, and Directional Movement. The inner sequential connection is determined by the fabrication characteristic of 3D printing. Figure 11 depicts the hierarchy relationship between these primitive operations. In order to infer the printer operations in each level, we extract the mechanism parameters of the printer (using status analysis functions) based on the data frames we obtained. After that, we integrate all the information we obtain into parameter sequences in time series. In detail, we describe the parameter extraction steps as follows:

- **Layer Movement Analysis:** For each data frame, we first determine whether it refers to the nozzle operation in the X-Y plane or the platform movement in the Z axis. Note that the actuation system for the platform is very different from the one for the nozzle because it contains a deformed bar instead of the belt. Therefore, platform movement generates unique acoustic signal. As a result, we apply acoustic channel model in this step.
- **Header Movement Analysis:** When the header prints with a regular printing speed, it continuously extrudes melted material. The extrusion unit speed is specifically determined by the layer height and the material. When the header performs a quick alignment, the material is no longer extruded and a much faster speed is

applied to avoid the stringing effect [5]. The fast movement generates the acoustic signal with a significant pattern. Hence, acoustic channel model is employed in this step to predict the header status and further infer whether the material needs to be extruded.

- **Axial Movement Analysis:** If the nozzle movement is in the X-Y plane, we need to further distinguish which axis the nozzle moves along with. Based on the preliminary result in Section 3, we find that the acoustic side channel performs well in predicting the nozzle axial movement.
- **Directional Movement Analysis:** Once knowing the specific axis the movement occurs, we investigate the moving direction in the last step. Based on the discussion in Section 4.1, we adopt the magnetic channel model to infer the directional information in the X or Y axis.
- **Integration:** Eventually, we obtain the predicted printer operation parameters (Time stamp/Distance/Device info) in each frame. We integrate all the information and generate the printer parameter set in time series.

Algorithm 1 G-code Reconstruction Algorithm

Input: A : printer status set in time series

v_{align} : particular aligning speed

v_{print} : particular printing speed

v_z : particular platform speed

win : frame size

Output: G-code: Reconstructed IP information

```

1: for each  $Frame_i$  do:
2:    $flag_x, flag_y, flag_z, x_{dir}, y_{dir}, flag_{align} \leftarrow a_i$  // Get
   params
3:    $d_x, d_y, d_z, d_e, tmp_v = 0$  // Initialize
4:   if  $flag_z = 1$  then // Z movement
5:      $tmp_v = v_{print}$ 
6:      $d_z = tmp_v * win$ 
7:      $P_z = P_z + d_z$ 
8:   else // XY movement
9:      $tmp_v = 0$ 
10:    if  $flag_{align} = 1$  then // Align
11:       $d_e = 0$ 
12:       $tmp_v = v_{align}$ 
13:    else // Print
14:       $d_e = e_{const}$  // Machine Specific
15:       $tmp_v = v_{print}$ 
16:    end if
17:    if  $flag_x = 1$  then // Move in X
18:       $d_x = x_{dir} * v_{print} * win$ 
19:       $P_x = P_x + d_x$ 
20:    else // Move in Y
21:       $d_y = y_{dir} * v_{print} * win$ 
22:       $P_y = P_y + d_y$ 
23:    end if
24:     $L_e = L_e + d_e$ 
25:  end if
26:  G-code  $\leftarrow G1, X : P_x, Y : P_y, Z : P_z, E : L_e, F :$ 
    $tmp_v$ 
27: end for
  
```

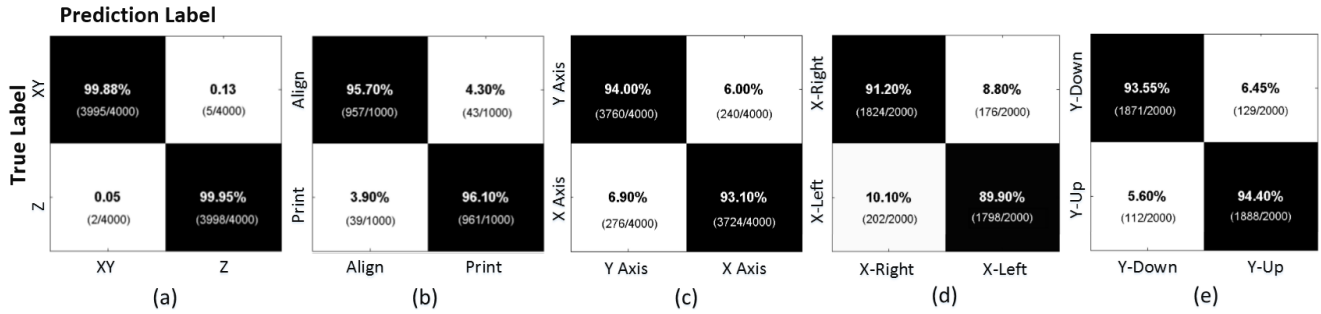


Figure 12: The classification results of operation models. (a) Layer Movement Model; (b) Head Movement Model; (c) Axial Movement Model; (d) X Directional Movement Model; (e) Y Directional Movement Model.

We employ the supervised learning model, support vector machines (SVM), as the classifiers to predict the primitive movement. More specifically, we use the Sequential Minimal Optimization (SMO) implementation of SVM which is provided in the Weka machine learning toolkit [4].

5.3 IP Reconstruction

IP reconstruction is a procedure which converts the printer status set in time series to the G-code format using an IP conversion function. Since the G-code combines both the printer mechanical and the object-related information, we develop a G-code reconstruction algorithm (ALGORITHM 1) to derive the IP from the printer status set.

6. EVALUATION

In this section, we analyze the performance of the primitive models and evaluate our method in the real-case study.

6.1 System Setup

As previously shown in Figure 8, the 3D printers we employ in this study are *Ultimaker 2 Go*, one of the most used open-source 3D printers in the market [9]. Our approach is also compatible with other FDM-type 3D printers, such as MakerBot Replicator [2] since they share the same mechatronic architecture. The smartphone, Nexus 5 [1] is equipped with multiple built-in sensors, including microphone with Qualcomm WCD9320 audio codec [8] and Asahi Kasei 3D Magnetometer Sensor AK8963 [6].

To collect the side-channel information, we implement a data recording application with Android OS v6.01. The smartphone is placed near the printer (within 20cm) to collect the audio and magnetic data while the printer is working. Both the printer and the smartphone’s built-in sensor have their own coordinates and configurations. Specifically, the audio data is recorded in mono channel with a sampling frequency of 44.1kHz and the encoding rate of 16 bit. The magnetic data, on the other hand, is collected with a sampling frequency of 100Hz in the unit of micro-Tesla (μT). The configuration of the printing speed determines a trade-off between the product yield and the time efficiency. Faster printing speed can improve the time efficiency yet reduce the product quality. In our work, we aim to ensure the high quality of printed product. Therefore, we set the nozzle printing speed as 180 mm/min and the alignment speed as 7800 mm/min.

6.2 Quantitative Accuracy Analysis

In this part, we address the concerns in two aspects: 1) What is the performance of each primitive operation model? 2) What is the performance variation of each model with different parameter settings?

6.2.1 Primitive Operation Models

We first apply Savitzky-Golay filter on the side-channel data and segment the signal into separate frames with a fixed frame size of 200 ms. Then we partition the operation frames into the training and testing set according to different models. Figure 12 shows the classification results.

Figure 12(a) is Layer Movement Model, which determines whether the printer prints in the X-Y plane or moves the platform in the Z axis. The training set involves 2000 magnetic frames in each category and the testing set includes 4000 magnetic frames in total. The model can differentiate the two operations with an average accuracy of 99.92%. The mechanical difference in two sets of actuation system provides rich operation information in the acoustic data.

Figure 12(b) is Head Movement Model, which detects whether the nozzle is printing or aligning in the X-Y plane. Specifically, acoustic side channel is utilized in the model training. The training and testing set both contain 1000 audio frames (half in each type). The result shows that 95.7% and 96.1% of the testing data are correctly classified in each group. As a result, we can infer whether the machine extrudes material in each timestamp.

Figure 12(c) is Axial Movement Model, which is used to predict whether the nozzle moves along the X or Y axis. The training set involves 2000 magnetic and audio frames of the X and Y axial movement (half in each direction) respectively. Afterwards, we verifies the model with 4000 testing frames. The confusion matrix indicates that the overall accuracy of the model reaches 93.55%.

Figure 12(d)(e) are X and Y Directional Movement Model respectively. In one axis, we train the corresponding model upon 1000 magnetic frames for each direction (2000 in total). We validate the performance by applying the model on the test set of 4000 frames. The confusion matrix shows that the model correctly classifies the moving direction of 90.55% frames in the X axis. Correspondingly, the accuracy in the Y axis achieves 93.98%.

6.2.2 Model Performance and Frame Size

Frame size is an important factor that directly affects the performance of the models. Small frame size increases the

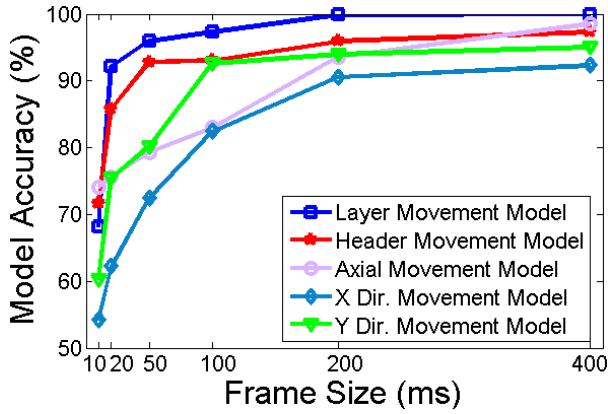


Figure 13: The accuracy results of the primitive operation models in 3D printing with different frame sizes.

temporal resolution, enabling us to reconstruct the printing process in fine-grained detail. However, it will correspondingly reduce the frequency resolution in spectral features, which could eventually lower the classification accuracy. As a result, we explore the performance of the models under different frame sizes. As depicted in Figure 13, the performance of the models gradually improve with the increase of the frame size. Larger frame size means there are more characteristic information contained in each frame, hence the data frame will be more accurately deduced in the high dimensional feature domain. Based on the performance tendency showed in the graph, we select the frame size of 200 ms in our evaluation.

6.3 Real World Evaluation

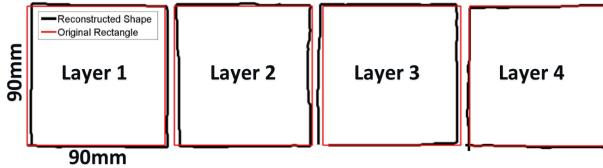


Figure 14: The reconstructed shape based on the magnetic-enhanced side-channel attack. The rectangle in red line is the designed shape in each layer. The shape in black line is the reconstructed one.

To evaluate our approach upon the real printing scenario, we first select rectangle as a regular shape since it involves all the primitive operations. Specifically, we generate a G-code file for a four-layer object, each layer of which is a 90mm*90mm rectangle and in the height of 1mm. The reconstructed shapes in each layer are depicted in Figure 14. In each layer, the reconstructed shape fits the original rectangle in general. There are outliers in the reconstructed ones due to the mis-classification in certain operations. Most outliers are in the Y axis. Such offsets (e.g. in Layer 1, 3) are generated by the mis-classifications in the previous X directional movements. This result is in coherence with the observation that the Y Directional Movement Model performs better than the X Direction Movement Model (see Section 6.2.1).

We introduce an error metric to evaluate the reconstruction performance in 3D printing attacks. The traditional error metrics, such as Mean Square Error Metrics [16] and Quadric Error Metrics [20], cannot quantify the true geometric error because these metrics consider each reconstructed point independently and estimate the error according to the *absolute* difference. In this case, local sparse outliers (e.g., a large error on a single segment) or global offsets will bias the entire quality value.

We argue that the error metric in 3D printing attack applications should reflect the global reconstruction quality and estimate the error according to the relative distortions. For example, the error from certain rigid transformation effects, such as translation, can be eliminated in the error metric because they will not alter the IP information. Therefore, we propose the Mean Tendency Error (MTE), which assesses the geometrical reconstruction based on the *relative* shape difference. Specifically, MTE is a geometric similarity descriptor that calculates the direction consistency between the design pattern and reconstructed pattern. It is formulated as:

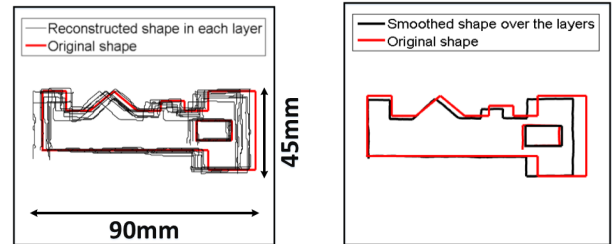
$$MTE = \frac{1}{n} \sum_{i=2}^n \{ |GX_i - GX_{i-1}) - (HX_i - HX_{i-1})| + |(GY_i - GY_{i-1}) - (HY_i - HY_{i-1})| \}, \quad (15)$$

where n is the number of sample points, GX, GY are the reconstructed points and HX, HY are the original points.

	Layer1	Layer2	Layer3	Layer4	Avg.
MTE	6.06%	7.12%	5.71%	4.57%	5.87%

Table 2: The MTE results of four layers when reconstructing the regular design.

Table 2 shows the calculated MTE for each layer respectively. The results range from 4.57% to 7.12%, with an average MTE of 5.87%. The low MTE over different layers indicates that the attack method can accurately and robustly reconstruct the original design IP.



(a) The original shape of the complex design and the reconstructed results of ten layers.

(b) The result after applying Layer Smooth Algorithm on all layers.

Figure 15: The demonstration of the reconstructed IP on a complex design.

The real complex design usually contains free-form segments and inner structures (e.g., a hollow structure can lead to multiple contours in the same layer), which traditional 3D scanning cannot detect. Free-form segments can be represented by a series of motion primitives in X, Y and Z directions. Inner structures can also be reconstructed by the proposed method because it can recognize the alignment in printing.

We test the attack approach on a complex shape. Specifically, the designed object contains ten layers (layer height is 1mm) and the contour dimension in each layer is 90mm*45mm. As shown in Figure 15(a), the original complex shape is colored in red and the reconstructed result in each layer is plotted in black. The triangle shape is reconstructed by a set of primitive movements in X and Y. Overall, the shape drift in the X axis is smaller than the one in the Y axis, which means that the Y axis movements are better predicted. In detail, the performance for X Directional Movement Model and Y Directional Movement Model is 89.83% and 93.67% in accuracy, respectively.

	Layer1	Layer2	Layer3	Layer4	Layer5
MTE	8.36%	8.97%	7.14%	8.77%	10.15%
	Layer6	Layer7	Layer8	Layer9	Layer10
MTE	15.87%	10.64%	8.35%	9.83%	8.64%

Table 3: Calculated MTE of each reconstructed layer for the complex shape.

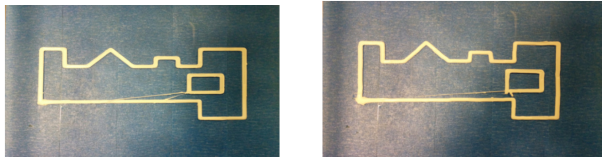
Algorithm 2 Layer Smooth Algorithm

Input: **Layer:** G-code for each layer in time series $t = 1, \dots, n$ **L:** Layer number
Output: *result*: G-code of the smoothed layer contour upon all layers in time series

- 1: **for** $t = 1 \rightarrow n$ **do**: // in each time stamp
- 2: $smoothX_i = \frac{1}{L} \sum_{k=1}^L \mathbf{Layer}_k(x)$
- 3: $smoothY_i = \frac{1}{L} \sum_{k=1}^L \mathbf{Layer}_k(y)$
- 4: **end for**
- 5: *result* $\leftarrow [smoothX; smoothY]$ //integrate the smooth result

We can observe that most reconstructed layers are similar to the original contour. The MTE results for the reconstructed layers are calculated in Table 3. The mean MTE upon the entire ten layers is 9.67%, with a standard deviation of 2.40%. To address the variation between the layers, we perform Layer Smooth Algorithm (ALGORITHM 2) to adjust the contour outliers.

The post-processing result is displayed in Figure 15(b). The algorithm well regulates the abnormal outliers in particular parts and generates a smooth contour similar to the original shape. The real printed objects is exhibited in Figure 16.



(a) The original designed complex shape.

(b) The replicated object based on the smoothed reconstruction result.

Figure 16: The real demonstration of the original design and the replicated one based on the reconstructed IP.

6.4 Practice Enhancement

In this above setting, we keep the orientation of the smartphone in both the training and attacking scenarios. For the sake of the attack feasibility, we explore a software solution to grant the side-channel data with the orientation-independent characteristics. With this approach, the training and attacking scenarios are not necessary to be performed with the same smartphone orientation. Considering the mono audio signal propagates in sphere and is naturally independent of orientation, we focus on the magnetic side-channel measures.

According to Euler’s rotation theorem [22], any rotation of a rigid structure in three dimensions can be represented as a combination of a vector \vec{u} and a scalar θ . Specifically, the rotation vector represents a rotation angle around a specified axis and is usually encoded in the form of unit quaternion [18, 33]. In Android OS, the rotation vector can be derived from a combination of sensor data from 6-axis accelerometer, 6-axis gyroscope (Invensense MPU-6515 [7]) and 3-axis magnetometer. The result is returned by sensor service *Sensor.TYPE_ROTATION_VECTOR*. A typical function, *getQuaternionFromVector()*, converts the rotation vector to a normalized quaternion. Therefore, the rotation matrix R can be calculated as:

$$\begin{pmatrix} a^2 + b^2 - c^2 - d^2 & 2bc - 2ad & 2bd + 2ac \\ 2bc + 2ad & a^2 - b^2 + c^2 - d^2 & 2cd - 2ab \\ 2bd - 2ac & 2cd + 2ab & a^2 - b^2 - c^2 + d^2 \end{pmatrix}, \quad (16)$$

where normalized quaternion q is:

$$q = a + \mathbf{bx} + \mathbf{cy} + \mathbf{dz}, |q| = 1. \quad (17)$$

Therefore, by applying the rotation matrix R upon the magnetic data in smartphone-frame orientation, we can achieve the orientation-independent data in world-frame orientation:

$$magData_{rot-free} = R * magData_{original}. \quad (18)$$

To evaluate the orientation-independent solution, we employ different rotation angles and record the normalized quaternion q , which remains constant when the smartphone is placed in a particular orientation. The converted magnetic data in each axis is calculated based on the equations above.

Angle	Mean Mag_x	Mean Mag_y	Mean Mag_z
0°	10.0244	38.0156	-51.7069
30°	10.2021	37.7480	-52.0877
60°	10.2554	37.9613	-51.3041
90°	10.1768	38.2078	-52.3945
Angle	Var. Mag_x	Var. Mag_y	Var. Mag_z
0°	-	-	-
30°	+1.77%	-0.70%	-0.74%
60°	+2.3%	-0.14%	-0.78%
90°	+1.52%	+0.51%	+1.33%

Table 4: The converted magnetic data with different rotation angles.

As shown in Table 4, the converted magnetic data remains stable in each axis while the smartphone’s orientation changes. The average variations are +1.87%, -0.11%, +0.43% respectively in each axis. In this way, we are able to

achieve the orientation-independent magnetic data regardless of the smartphone rotation.

7. DISCUSSION

In this section, we discuss the current limitations and then describe the future work.

Distance Effect: Attack effectiveness highly depends on the side-channel range. Compared to the acoustic side channel, the effective magnetic side channel diminishes much faster ($\propto \frac{1}{r^3}$). We evaluate the attack effectiveness with three different distance setups, i.e., 20cm, 30cm and 40cm, respectively. Reconstruction results are shown in Table 5.

	Dist. 20cm	Dist. 30cm	Dist. 40cm
Avg. MTE	5.87%	12.94%	34.45%

Table 5: The average (avg.) MTE of the reconstructed rectangle when different distances (dist.) are applied.

It depicts that the reconstruction performance deteriorates rapidly when the distance from smartphone to printers increases (as low as the 34.45% at the 40cm distance). Nevertheless, with the dramatic advancement of the sensors equipped on smartphones, the higher sensitivity will lead to longer effective attack range. Moreover, attacking with multiple smartphones is another direction to explore. Some work [35, 23, 44] have showed that multi-sensor fusion system can achieve more information in higher dimension, further enhance the signal-to-noise rate, and address certain limitations (e.g., distance) in the single-sensor system.

Print Speed Effect: Print speed is a critical factor to affect the fabrication quality. The best print speed is determined by the material thermoplastic property. In this study, we employ the PLA plastic filament, whose recommended print speed is 180 mm/min. Some emerging materials (e.g. soft hydrogel material) can have a quality print with a very fast velocity. In the future plan, we will evaluate the attack approaches on different print speeds. We expect the performance will reach a limit on some very fast print speed setup, and this limitation is caused by smartphone hardware specification (e.g., sampling frequency, sensor sensitivity).

Position Effect: The smartphone’s position has limited effect on the acoustic signal since the sound propagation is spherical and fast enough. The absolute magnetic signal, on the other hand, changes with regard to the magnetic field distribution around the 3D printer as well as the smartphone’s position. The directional pattern (Figure 9) might be inverse when the smartphone is moved to the other side of the 3D printer. In this case, training phase can be re-applied to ensure the effectiveness of the magnetic model.

Ambient Noise Effect: Ambient acoustic and magnetic noise will affect the performance of the prediction models. The affected degree is tightly related to the noise level. Light ambient noise can be removed using specific filters, such as the aforementioned Savitzky-Golay filter in Section 5.1. Strong, wide-width ambient noise will contaminate the side channels and can be applied as a potential mitigation method to decrease the attack performance, which is discussed in Section 8.2.

Carry-on Attack: Another enhanced practice is the carry-on attack model. In this threat model, the attackers can hide smartphone(s) in his pocket and stand around 3D printers. In Section 6.4, we introduce a solution to project the side-channel data into the world frame regardless of the smartphone’s orientation. This feature potentially enables this new and practical attack scenario. In the future work, we will evaluate the setup where the attacker places the smartphone in the pocket and stands or walks around the printer. The signal variation caused by body motion can be compensated by the built-in inertial sensors [43].

Advanced Shape Exploration: Due to the elegant concept of layer by layer fabrication, 3D printers can build complicated objects with a wide variety of materials and functions. We plan to evaluate the performance on various designs with a diverse shape complexity, such as circle, ellipse, arc and complex topology. The challenge on these complicated shapes is to accurately identify the printing state (e.g., material extruding or not) because the nozzle motion trajectory will become convoluted. The posted process, such as layer smooth algorithm (Algorithm 2), needs further proning.

8. DEFENSE MECHANISM

As shown in Figure 1, the 3D printing chain includes the software process (e.g., 3D design and G-code generation) and hardware process (e.g., physical manufacturing). We propose the possible defense methods in two types, e.g., software-based methods and hardware-based methods.

8.1 Software-based Methods

First, we would like to propose two software-based methods to mitigate the side-channel attacks. We highlight that these methods do not introduce hardware cost or alter the configuration of 3D printers.

- **Dynamic Path Planning:** To protect the 3D printing design IP from training-based attack method, we propose the dynamic path planning strategy. Generally, the operation models require an upfront training. Therefore, to degrade the performance of the prediction models, we adopt dynamic printing configurations in the process of G-code generation. For example, the printing speed for a specific material has a proper speed range based on the material’s characteristic. Applying different speed settings within the proper range in the printing process will maintain the yield but reduce the attack accuracy. Different temperature settings in the nozzle heater are also required to match the printing speed and will further generate additional interference in the side channels.
- **Dummy Task Injection:** As described in Section 5, the successful deduction on nozzle status (print and align) is determined by the nozzle speed. This model is based on the convention that nozzle moves faster on alignment than on printing. Based on this knowledge, we can consider to inject additional dummy tasks on purpose to spoof the sensors. Specifically, the dummy task comprises a set of random trajectories with the regular print speed yet no real material extrusion. The dummy task can be integrated in the process of G-code generation. This defense approach can increase

the print duration while have little impact on the print quality.

8.2 Hardware-supported Methods

Second, we discuss the hardware-supported methods to reduce the IP theft risk. Generally, we need to prevent the malicious attackers from collecting the valuable side-channel information.

- **Hardware Shielding:** The most straightforward strategy to limit the side-channel information emission is to physically isolate the side-channel sources by hardware shielding. There are a few off-the-shelf acoustic and electromagnetic shielding materials [25, 21] which are capable of eliminating the interference. However, shielding hardware brings additional hardware cost to the system and even decreases the operational usability in daily use.
- **Side Channel Interference:** Another hardware-based solution is to intentionally introduce more interference to affect the attacker’s sensors. Some home appliances (e.g., refrigerators, air-conditioners) can generate strong electromagnetic interference (EMI) to deteriorate the side-channel quality. Moreover, a few recent studies shows that sound noise can malfunction the MEMS based sensors [32, 36], which are widely used in smartphones. However, interference, such as EMI and sound noise, might raise the potential health concerns.

9. RELATED WORK

Understanding the vulnerability is the first step to build robust and resilient systems. As an emerging driving force in manufacturing, security issues in 3D printing have been raised in the past few years. As aforementioned, 3D printing chain involves both cyber-domain process and physical domain process. Since 2014, people start to investigate cyber vulnerabilities in the 3D printing chain. For example, Sturm *et al.* [38] examined specific malwares to conduct certain malicious operations to the digital files in the cyber domain and proved that the product yield was affected. Wells *et al.* [41] identified the issue of cyber vulnerability by designing malicious software to infect, modify or steal STL files or tool-path files.

On the contrary, physical attacks in the 3D printing chain remain underexplored. Backes *et al.* [14] inspected the acoustic emanations of dot matrix printers. They presented a side-channel attack method to recover what a dot matrix 2D printer is printing based on the sound record. Al Faruque *et al.* [12] demonstrated the acoustic side-channel attack on 3D printing. However, they only considered the cases with single contour instead of multiple ones. Moreover, both work employed professional audio equipment in the attacking approaches. 3D scanning [20, 27] is another technology to reconstruct the digital three-dimensional model by creating a point cloud of geometric samples on the surface of the object. Yet this technology is not capable of inner structure detection and the scanner, such as Matter And Form 3D scanner [3], still remains expensive. Also, 3D scanning attack requires the physical access to the 3D objects.

In the era of smart devices and internet of things, physical domain attacks leveraging cost-efficient and ubiquitous sensors deserve more attentions.

10. CONCLUSION

3D printing has been hailed as the third industrial revolution in the unique way that products are conceived, designed, manufactured and distributed to end users. However, there are still many security unknowns about using 3D printers in daily life, which might impose the potential risk on applied fields or hinder its applicability to more IP-sensitive industries. In this paper, we made the first step to understand the potential vulnerability in the 3D printing process in daily life. Specifically, we presented a smartphone-based side-channel attack that takes inputs of magnetic and acoustic emanations in the 3D printing process, and reconstructed the design object with high accuracy in regular and complex design inference. As demonstrated in our study, the IP attack is easy to launch and we discuss several approaches to mitigate the risk. We hope that the finding of this study can serve as the reference to understand and protect the 3D printer systems.

11. ACKNOWLEDGMENTS

We thank our shepherd Christina Poepper and the anonymous reviewers for their insightful comments on this paper. This work was in part supported by National Science Foundation grants CNS-1421903 and CNS-1547167.

12. REFERENCES

- [1] *Google Nexus 5 Smartphone*. <https://www.google.com/nexus/5/>.
- [2] *MakerBot Replicator*. <https://www.makerbot.com/>
- [3] *Matter And Form 3D Scanner*. <https://matterandform.net/scanner>.
- [4] *Weka Machine Learning Toolkit*. <http://www.cs.waikato.ac.nz/ml/weka/>.
- [5] *3D Printing Stringing Effect*. 2015. <https://ultimaker.com/en/resources/19504-stringing>.
- [6] *Asahi Kasei 3D Magnetometer Sensor AK8963*. 2015. <http://www.akm.com/akm/en/product/datasheet1/?partno=AK8963>.
- [7] *InvenSense MPU6515 6-Axis Accelerometer and Gyroscope*. 2015. https://www.chipworks.com/TOC/InvenSense_MPU-6515_6-Axis_Accelerometer_Gyroscope_FAR-1401-901_TOC.pdf.
- [8] *Qualcomm WCD9320 audio codec*. 2015. <https://developer.qualcomm.com/download/sd600/wcd9311-audio-codec-device-specification.pdf>.
- [9] *Ultimaker 3D Printer*. 2015. <https://ultimaker.com/en/products/ultimaker-2-go>.
- [10] *Zoom H6 Handy Recorder*. 2015. <http://www.zoom-na.com>.
- [11] *G-code (RS-274)*. First edition in 1950s. <http://reprap.org/wiki/G-code>.
- [12] M. A. Al Faruque, S. R. Chhetri, A. Canedo, and J. Wan. Acoustic side-channel attacks on additive manufacturing systems. In *Proceedings of the ACM/IEEE Sixth International Conference on Cyber-Physical Systems*. ACM, 2016.
- [13] P. Anderson and C. A. Sherman. A discussion of new business models for 3d printing. *International Journal of Technology Marketing*, 2(3):280–294, 2007.
- [14] M. Backes, M. Dürmuth, S. Gerling, M. Pinkal, and C. Sporleder. Acoustic side-channel attacks on

- printers. In *USENIX Security Symposium*, pages 307–322, 2010.
- [15] D. Bak. *3D System Solutions*. Assem. Autom, 2004. <http://www.3dsystems.com/solutions/overview>.
- [16] T. Chai and R. R. Draxler. Root mean square error (rmse) or mean absolute error (mae)?—arguments against avoiding rmse in the literature. *Geoscientific Model Development*, 7(3):1247–1250, 2014.
- [17] G. A. Fielding, A. Bandyopadhyay, and S. Bose. Effects of silica and zinc oxide doping on mechanical and biological properties of 3d printed tricalcium phosphate tissue engineering scaffolds. *Dental Materials*, 28(2):113–122, 2012.
- [18] W. R. Hamilton. Ii. on quaternions; or on a new system of imaginaries in algebra. *The London, Edinburgh, and Dublin Philosophical Magazine and Journal of Science*, 25(163):10–13, 1844.
- [19] J.-U. Hou, D.-G. Kim, S. Choi, and H.-K. Lee. 3d print-scan resilient watermarking using a histogram-based circular shift coding structure. In *Proceedings of the 3rd ACM Workshop on Information Hiding and Multimedia Security*, pages 115–121. ACM, 2015.
- [20] A. Karasik and U. Smilansky. 3d scanning technology as a standard archaeological tool for pottery analysis: practice and theory. *Journal of Archaeological Science*, 35(5):1148–1168, 2008.
- [21] K&J Magnetic Inc. Mag Shielding Materials. <https://www.kjmagnetics.com/>.
- [22] J. B. Kuipers et al. *Quaternions and rotation sequences*, volume 66. Princeton university press Princeton, 1999.
- [23] C. Y.-K. Lai and P. Aarabi. Multiple-microphone time-varying filters for robust speech recognition. In *Acoustics, Speech, and Signal Processing, 2004. Proceedings.(ICASSP'04). IEEE International Conference on*, volume 1, pages I–233. IEEE, 2004.
- [24] T. Lambrou, P. Kudumakis, R. Speller, M. Sandler, and A. Linney. Classification of audio signals using statistical features on time and wavelet transform domains. In *Acoustics, Speech and Signal Processing, 1998. Proceedings of the 1998 IEEE International Conference on*, volume 6, pages 3621–3624. IEEE, 1998.
- [25] LESSEMF Inc. Shielding Fabrics. <http://www.lessemf.com/fabric.html>.
- [26] B. Leukers, H. Gülkan, S. H. Irsen, S. Milz, C. Tille, M. Schieker, and H. Seitz. Hydroxyapatite scaffolds for bone tissue engineering made by 3d printing. *Journal of Materials Science: Materials in Medicine*, 16(12):1121–1124, 2005.
- [27] M. Levoy, K. Pulli, B. Curless, S. Rusinkiewicz, D. Koller, L. Pereira, M. Ginzton, S. Anderson, J. Davis, J. Ginsberg, et al. The digital michelangelo project: 3d scanning of large statues. In *Proceedings of the 27th annual conference on Computer graphics and interactive techniques*, pages 131–144. ACM Press/Addison-Wesley Publishing Co., 2000.
- [28] Y. Liao, H. Li, and Y. Chiu. Study of laminated object manufacturing with separately applied heating and pressing. *The International Journal of Advanced Manufacturing Technology*, 27(7-8):703–707, 2006.
- [29] H. R. D. Market. Global industry analysis, size, share, growth, trends and forecast, 2013–2019, 2014.
- [30] J. H. Martin and D. Jurafsky. Speech and language processing. *International Edition*, 2000.
- [31] P. Mermelstein. Distance measures for speech recognition, psychological and instrumental. *Pattern recognition and artificial intelligence*, 116:374–388, 1976.
- [32] Y. Michalevsky, D. Boneh, and G. Nakibly. Gyrophone: Recognizing speech from gyroscope signals. In *23rd USENIX Security Symposium (USENIX Security 14)*, pages 1053–1067, 2014.
- [33] B. Rosenfeld. A history of non-euclidean geometry. 1988.
- [34] A. Savitzky and M. J. Golay. Smoothing and differentiation of data by simplified least squares procedures. *Analytical chemistry*, 36(8):1627–1639, 1964.
- [35] G. Shakhnarovich, L. Lee, and T. Darrell. Integrated face and gait recognition from multiple views. In *Computer Vision and Pattern Recognition, 2001. CVPR 2001. Proceedings of the 2001 IEEE Computer Society Conference on*, volume 1, pages I–439. IEEE, 2001.
- [36] Y. Son, H. Shin, D. Kim, Y. Park, J. Noh, K. Choi, J. Choi, and Y. Kim. Rocking drones with intentional sound noise on gyroscopic sensors. In *24th USENIX Security Symposium (USENIX Security 15)*, pages 881–896, 2015.
- [37] S.-J. Song, J. Choi, Y.-D. Park, S. Hong, J. J. Lee, C. B. Ahn, H. Choi, and K. Sun. Sodium alginate hydrogel-based bioprinting using a novel multinozzle bioprinting system. *Artificial organs*, 35(11):1132–1136, 2011.
- [38] L. Sturm, C. Williams, J. Camelio, J. White, and R. Parker. Cyber-physical vulnerabilities in additive manufacturing systems. *Context*, 7:8, 2014.
- [39] J. Thilmann. Printed life. *Mechanical engineering*, 134(1):44, 2012.
- [40] W.-H. Tsai, Y.-M. Tu, and C.-H. Ma. An fft-based fast melody comparison method for query-by-singing/humming systems. *Pattern Recognition Letters*, 33(16):2285–2291, 2012.
- [41] L. J. Wells, J. A. Camelio, C. B. Williams, and J. White. Cyber-physical security challenges in manufacturing systems. *Manufacturing Letters*, 2(2):74–77, 2014.
- [42] T. Wohlers. *Wohlers report 2015: 3D Printing and Additive Manufacturing State of the Industry*. Wohlers Associates, 2015.
- [43] H. Zhao and Z. Wang. Motion measurement using inertial sensors, ultrasonic sensors, and magnetometers with extended kalman filter for data fusion. *Sensors Journal, IEEE*, 12(5):943–953, 2012.
- [44] E. Zwysig, F. Faubel, S. Renals, and M. Lincoln. Recognition of overlapping speech using digital MEMS microphone arrays. In *Acoustics, Speech and Signal Processing (ICASSP), 2013 IEEE International Conference on*, pages 7068–7072. IEEE, 2013.